NONLINEAR RESPONSE OF A VERY FLEXIBLE AIRCRAFT UNDER LATERAL GUST

Alfonso del Carre[1], Patricia Teixeira[2], Rafael Palacios[1], and Carlos E.S. Cesnik[2]

[1]Dept. of Aeronautics, Imperial College London
Exhibition Road, SW7 2AZ London, UK
alfonso.del-carre14@imperial.ac.uk

[2] Department of Aerospace Engineering, University of Michigan
1320 Beal Avenue, Ann Arbor, MI, 48109, USA

Keywords. Nonlinear aeroelasticity, very flexible aircraft, flight dynamics, gust response, lateral gust, computational aeroelasticity

Abstract. The coupled aeroelastic-flight dynamic response of very flexible aircraft to discrete lateral gusts is investigated using two independent state-of-the-art simulation and analysis frameworks. They are both built by coupling a geometrically-nonlinear composite beam finite-element discretization of the primary slender structures and a thin-surface unsteady vortex-lattice approximation to the potential-flow aerodynamic equations. Results are presented for the University of Michigan X-HALE unmanned aerial vehicle configuration, and show very good comparison between the two simulation tools, thus working as a partial verification of their implementation, while providing some new insights into the simulation requirements for complex nonlinear response of very flexible aeroelastically-driven aircraft.

1 INTRODUCTION

Recent advances in electric propulsion, carbon-fiber manufacturing, and communications systems have led to the development of High Altitude Long Endurance (HALE) air vehicles. The efficiency demand that this kind of aircraft poses results in very light structures and high-aspect-ratio wings. Many HALE configurations, particularly solar-powered systems, present a large fraction of their mass distributed along the wing span. When wing deflections take place, the overall center of mass can be significantly displaced. These very slender wings also present low natural frequencies and can be subject to high deformations in a wide range of scenarios, thus leading to fully-coupled nonlinear aeroelastic-flight dynamic responses [1].

The response of the aircraft to lateral gusts is a particularly challenging problem, as loads are typically driven by wing dihedral on conventional aircraft. On very flexible platforms, an effective (and dynamic) dihedral appears due to the large-amplitude time-varying wing displacements, and results in more complex loading scenarios and potentially new structural integrity risks to the aircraft, particularly during the landing phase. They are further complicated by the deflections that the lateral gust may generate on the wake of the propellers and their subsequent interactions with downstream surfaces. Neither of those effects are captured by standard linear analysis methods in aeroelasticity.

Lateral gust conditions are included in air vehicle certification and typically size vertical tail plane on a conventional wing-body-tail configuration. However, its influence on the

Figure 1: The X-HALE on the ground (left) and in flight shortly after take off (right). Images from [4].

dynamic loading and behaviour of very flexible, non-conventional configurations is yet to be studied in depth. In particular, certification procedures usually assume that modal aeroelastic solvers are used for gust response analysis. A part of the CS-25 Advisory Circular from the FAA concerning the Dynamic Gust Loading [2] states that gust limit loads shall be computed by decoupling steady $1 - g$ loading and gust incremental loads. It also states that *a linear elastic structural model and a linear (unstalled) aerodynamic model are normally recommended as conservative and acceptable for the unaugmented airplane elements of a loads calculation*. While very flexible HALE-like platforms are not covered by CS-25, the lack of historical precedent implies that design teams may still rely on those guidelines for structural sizing.

To address the lack of guidelines, this paper carries out a numerical investigation on the open-loop nonlinear aeroelastic response of very flexible aircraft to lateral gusts using the University of Michigan X-HALE unmanned aerial vehicle as the reference configuration [3]. Two different time-domain simulation environments are used, both built around geometrically-nonlinear composite beams with unsteady vortex-lattice aerodynamics and therefore suited to this problem. However, they consider different spatial and time discretizations as well as coupling schemes. A code-to-code comparison supports the verification of the implementation for this rather complex configuration and will also facilitates the identification of bottlenecks in the numerical strategies.

The X-HALE UAS (Fig. 1) has been developed at the Active Aeroelasticity and Structures Research Laboratory at the University of Michigan. It serves as a nonlinear aeroelastic testbed intended for code validation and controller development for very flexible aircraft. Its main wing is composed of 6 panels of constant structural and aerodynamic properties, with a 10 degree dihedral region on the outer panels. The center tail is actuated along the longitudinal axis and it can be rotated to act either as a horizontal or vertical tail. The remaining four tails (two on each semi-span) act as elevators, deflecting uniformly. Three ventral fins, between the wing and the center and inboard tails, are also present to augment the lateral stability of the X-HALE. Five propellers, one located at each pod, provide thrust. These pods also contain the avionics equipment, battery packs, instrumentation, as well as the landing gear. X-HALE presents an aspect ratio of 30, with a relative tip deflection of approx. 18% of its semi-span under nominal cruise conditions [3] and even larger tip deflections during manoeuvres or gust conditions.

This configuration is a representative testbed of more complex HALE aircraft due to its multiple tails, low weight, high flexibility and aspect ratio, span-distributed mass and span-distributed propulsion [5].

2 NUMERICAL METHODS

The two solvers used here are SHARPy[1] (Simulation of High Aspect Ratio Planes in Python) developed at Imperial College London [6–9] and UM/NAST (University of Michigan's Nonlinear Aeroelastic Simulation Toolbox) [10–12]. Both solvers are built on geometrically-nonlinear composite beam structures coupled with medium-fidelity unsteady aerodynamic solvers.

2.1 SHARPy

SHARPy is a Python-based tool released under an open-source license. It is designed as an nonlinear aeroelastic simulation framework for design and analysis of aeroelastic configurations and their controllers. The main solver is a time-domain, geometrically nonlinear coupled solver with a Block Gauss-Seidel iteration scheme between the structural and aerodynamic solutions.

The resulting system from solving Hamilton's principle in its strong form applied on an homogenized composite structure with linear constitutive equations and nonlinear velocity-displacement kinematic relations is then discretized with quadratic 1-D finite elements [7]. Being $\boldsymbol{\eta}$ the state variable containing the displacements and rotations and $\boldsymbol{\mathcal{N}}$ the shape functions, we have: $\boldsymbol{\eta} = \boldsymbol{\mathcal{N}}\bar{\boldsymbol{\eta}}$, where the displacements are expressed in body-attached frame of reference, A and the nodal rotations are parametrized using Cartesian Rotation Vectors (CRV). The rewritten Hamilton's principle results in

$$\boldsymbol{\mathcal{M}}_{\eta}(\bar{\boldsymbol{\eta}})\ddot{\bar{\boldsymbol{\eta}}} + \boldsymbol{m}_{a}(\bar{\boldsymbol{\eta}}) \left\{ \begin{array}{c} \dot{\boldsymbol{v}}_{A} \\ \dot{\boldsymbol{\omega}}_{A} \end{array} \right\} + \boldsymbol{\mathcal{F}}_{\mathrm{gyr}}(\bar{\boldsymbol{\eta}}, \dot{\bar{\boldsymbol{\eta}}}, \boldsymbol{v}_{A}, \boldsymbol{\omega}_{A}) + \boldsymbol{\mathcal{F}}_{\mathrm{stif}}(\bar{\boldsymbol{\eta}}) = \boldsymbol{\mathcal{F}}_{\mathrm{ext}}, \tag{1}$$

Where $\boldsymbol{\mathcal{M}}_{\eta}$ is the tangent mass matrix, $\boldsymbol{m}_{a}$ is the rigid body mass matrix, $\boldsymbol{v}_{A}$ and $\boldsymbol{\omega}_{A}$ are rigid body linear and rotation velocities respectively, and $\boldsymbol{\mathcal{F}}_{\mathrm{gyr}}$, $\boldsymbol{\mathcal{F}}_{\mathrm{stiff}}$, and $\boldsymbol{\mathcal{F}}_{\mathrm{ext}}$ are the discrete gyroscopic, elastic and external forces (including aerodynamic forces) respectively. This equation is then solved iteratively using a fixed-point iteration scheme. Time integration is carried out with an explicit Newmark-β formulated in incremental form. Being $\boldsymbol{\eta}^{k}$ the state vector at the k-th iteration and $\Delta\boldsymbol{\eta}^{k}$ the increment from the Newmark-β iterative process, the next iteration state vector is given by:

$$\boldsymbol{\eta}^{k+1} = \boldsymbol{\eta}^{k} + \Delta\boldsymbol{\eta}^{k+1}. \tag{2}$$

The convergence residual is defined as

$$\epsilon^{k} = \|\Delta\boldsymbol{\eta}^{k}\| / \|\Delta\boldsymbol{\eta}^{0}\|. \tag{3}$$

Additionally, an absolute convergence threshold is implemented for cases where the initial state is close to the converged solution. It is important to note that the flight dynamics are solved monolitically with the flexible degrees of freedom. This ensures the gyroscopic forces are instantly updated every FSI iteration, accelerating the aeroelastic problem convergence.

The beam solver is implemented as a library in Fortran 2008 and with LAPACK or Intel MKL as a linear algebra engine.

[1] http://github.com/imperialcollegelondon/sharpy

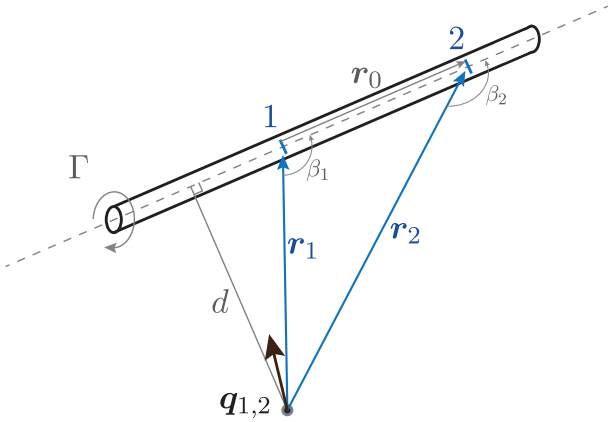

Figure 2: Definition of the variables used to evaluate the Biot-Savart law.

The aerodynamic solver is an Unsteady Vortex Lattice Method [13]. Once grid geometry ($\boldsymbol{\zeta}$) and circulations (Γ) are defined, the instantaneous induced velocity field at a point of coordinates $\boldsymbol{x}$ can be written as

$$\boldsymbol{u}(\boldsymbol{x},t) = \boldsymbol{\mathcal{A}}^3\left(\boldsymbol{x},\boldsymbol{\zeta}(t)\right)\boldsymbol{\Gamma}(t) + \boldsymbol{\mathcal{A}}^3_w\left(\boldsymbol{x},\boldsymbol{\zeta}_w(t)\right)\boldsymbol{\Gamma}_w(t). \tag{4}$$

The AIC matrices ($\boldsymbol{\mathcal{A}}^3$, $\boldsymbol{\mathcal{A}}^3_w$) are computed applying a variant of the Biot-Savart law with a cutoff vortex model. Applying it to obtain the velocity induced by a finite linear vortex segment from $\boldsymbol{r}_1$ to $\boldsymbol{r}_2$ yields

$$\begin{aligned}
s_V &= \frac{1}{2}\left(r_1 + r_2 + r_0\right) \\
a_V &= 2\frac{\sqrt{s_v(s_v - r_1)(s_v - r_2)(s_v - r_0)}}{\epsilon_{OT} + r_0} \\
\boldsymbol{q}_{1,2} &= \begin{cases} 0 & \text{if } a_V < r_c \\ \dfrac{\Gamma}{4\pi}\dfrac{\boldsymbol{r}_1 \times \boldsymbol{r}_2}{\left|\boldsymbol{r}_1 \times \boldsymbol{r}_2\right|^2 + \epsilon_{OT}}\boldsymbol{r}_0\left(\dfrac{\boldsymbol{r}_1}{r_1 + \epsilon_{OT}} - \dfrac{\boldsymbol{r}_2}{r_2 + \epsilon_{OT}}\right) & \text{if } a_V \geq r_c \end{cases}
\end{aligned} \tag{5}$$

where ϵ_{OT} is chosen to be as low as $\mathcal{O}(10^{-10})$ in order to avoid numerical-precision singularities when $d \to 0$, and the vortex radius r_c is specified as a ratio of r_0. All the simulations here shown have been run with $r_c = 10^{-3}$. The remaining terms are defined in Figure 2.

The behaviour of the Biot-Savart law evaluation routine when $d \to 0$ is critical in dynamic simulations with wake-lifting surface intersection. The aircraft model used for this paper has three surfaces located in the same plane and aligned with the free stream.

Another important point when considering lateral flight dynamics is the force evaluation in the UVLM. The classic approach, described by Katz and Plotkin [14], relies on the assumption of aligned panels with the flow. This method does not capture the lateral component of the incident velocity effect on the forces. The method here implemented is described by Simpson *et al.* [15]. The aerodynamic forces can be split in two contributions: steady and unsteady. The steady forces $\boldsymbol{f}_{\text{st}}$ are computed as

$$\delta\boldsymbol{f}_{\text{st}} = \rho_\infty\Gamma\left(\boldsymbol{U} \times \delta\boldsymbol{\ell}\right) \tag{6}$$

whereas the unsteady contribution, $\boldsymbol{f}_{\text{unst}}$, is

$$\delta \boldsymbol{f}_{\text{unst}} = \rho_\infty \frac{\partial \Gamma}{\partial \text{t}} c \left(\hat{\boldsymbol{U}} \times \delta \boldsymbol{\ell} \right), \tag{7}$$

where ρ_∞ is the free stream density, Γ is the vortex ring circulation, $\boldsymbol{U}$ is the incoming flow velocity, and $\hat{\boldsymbol{U}}$ its associated unit vector. c is the panel chordwise dimension and $\boldsymbol{\ell}$ is the vortex ring segment vector.

The unsteady contribution can be understood as the added mass effects. Numerical studies carried out by the authors have shown that in some cases, its contribution cannot be dismissed. This is specially true in the case of HALE configurations, where wing loading is very low, with low mass as well. However, the numerical implementation of this term involves some work to avoid numerical divergence, and it relies on finite differences to calculate the $\partial\Gamma/\partial\text{t}$ term.

The UVLM implementation is an in-house library written in C++14 that heavily relies on the Eigen library [16]. The main advantage of this library is that is has been developed from scratch with multi-language interfacing in mind. The main result of this is that the UVLM is solved using the existing data in the Python part of the code, with no need for data duplication. This is especially important due to the large number of functions calls that might be needed during the FSI iteration. The UVLM library supports different wake modeling levels. From an infinite single horseshoe vortex until a discretized wake convected with the background flow and the other vortices velocities contributions. This last method results in a rolled up wake, which in some wake-tail interference cases might be relevant for the overall flight dynamics.

SHARPy relies on a strongly coupled FSI scheme based on a Block Gauss-Seidel method. Residuals for both structural displacements and rotations, and velocities are used for assessing convergence in the FSI loop. While weakly coupled simulations can be run by performing a single FSI iteration, many nonlinear interactions require a strongly coupled scheme to be captured.

The final solver is a highly modular framework with both linear and non linear capabilities. Other more complex aeroelastic simulations such as catapult take off procedures [9] and low-altitude flight in a realistic LES 3D boundary layer have been already run.

The results obtained with SHARPy and included in this paper are set up with the same numerical parameters. From the structural side, the geometrically nonlinear beam equations are iterated until the residual ϵ^k defined in equation (3) falls below 10^{-6}. The parameter controlling the artificial damping in the time integrator is set at $\beta = 10^{-2}$.

For problems with large apparent mass effects, the $\dot{\Gamma}$ term in equation (7) is filtered before being used for the evaluation of the unsteady forces in order to avoid numerical instabilities when coupling the structural and aerodynamic solvers. The filter used is a Wiener filter [17] with a window length of $7\Delta t$. It has been chosen due to its capability of estimating the noise of the signal without user input. The implementation used in SHARPy is integrated in SciPy. The wake is convected using the background flow, while the vortex-induced velocity influence is not calculated. This allows to speed up the computations while retaining enough information to capture wake-surface interactions.

The Fluid-Structure Interaction (FSI) Block Gauss Seidel iteration residual is defined as

$$\epsilon_{\text{FSI}}^{k} = \max\left(\frac{\left\|\boldsymbol{\eta}^{k} - \boldsymbol{\eta}^{k-1}\right\|}{\|\boldsymbol{\eta}^{0}\|}, \frac{\left\|\dot{\boldsymbol{\eta}}^{k} - \dot{\boldsymbol{\eta}}^{k-1}\right\|}{\|\dot{\boldsymbol{\eta}}^{0}\|}\right), \tag{8}$$

where $\boldsymbol{\eta}$ is the structural state vector including displacements, rotations and rigid body motions and orientations, while $\dot{\boldsymbol{\eta}}$ is its time derivative. These results have been converged with $\epsilon_{\text{FSI}} < 10^{-6}$. In order to avoid numerical divergence in the FSI iteration process and speed up the convergence process, a relaxation process is carried out every FSI iteration. At the k-th iteration, the structural forces obtained with the aerodynamic solver are noted as $\bar{F}^{k}$, while the relaxed forces that go in the structural solver are

$$F^{k} = (1 - \omega_{\text{FSI}})\bar{F}^{k} + \omega_{\text{FSI}}\bar{F}^{k-1}. \tag{9}$$

$\omega_{\text{FSI}} \in [0, 1)$ is the relaxation factor. The cases shown here are run with an increasing relaxation factor, from 0.4 to 0.8, where ω_{FSI} grows linearly in 15 FSI iterations. The varying relaxation factor accelerates the convergence in the earlier iterations while damping oscillations between iterations if the current time step is converging slower than previous steps.

2.2 UM/NAST

The University of Michigan's Nonlinear Aeroelastic Simulation Toolbox (UM/NAST) [10–12, 18] was developed for the aeroelastic simulation of very flexible aircraft. UM/NAST employs a geometrically nonlinear structural formulation using a strain-based finite element [19]. Within each element, constant strains in extension, twist, and in- and out-of-plane bending are assumed, totalizing 4 degrees of freedom per element (the related displacements are obtained by post processing the strain results). The equations for structural dynamics, nonlinear 6 DoF vehicle dynamics and aerodynamics are integrated simultaneously using a weak coupling approach and three different numerical schemes options: implicit trapezoidal, generalized alpha and forward Euler schemes. The resulting system of equations to be solved has the following format [11]:

$$M(\epsilon)\ddot{q} + C(\epsilon, \dot{\epsilon})\dot{q} + Kq = R \tag{10}$$

where M, C and K represents the generalized mass properties, damping and stiffness matrices, respectively; $q = (\epsilon, p_B, \Theta_B)$ is a set of generalized coordinates containing the strains associated with the flexible vehicle, ϵ, the body inertial position, p_B, and an arbitrary orientation vector, Θ_B, of the body frame of reference;and R represents generalized forces accounting by aerodynamics loads, gravity, applied loads, etc.

Various aerodynamic models are available depending on the problem being analyzed. Originally a potential-flow finite state Peter's inflow aerodynamic model (2D strip theory) with a correcting factor for 3D effects was implemented [10–12]. More recently, a steady and unsteady Vortex Lattice solver (VLM) [20], as well as a reduced order model for transonic regimes were also added as aerodynamic options in the aeroelastic framework.

Although more expensive to run than the simple strip theory approach (yet much cheaper than RANS simulations), the VLM has the advantage of capturing mutual influence among lifting surfaces, the effect of wake and wake history and allows the modeling of

lifting surfaces subject to large and arbitrary structural displacements. Assuming potential flow and applying vortex ring elements distributed along panels and wake panels of lifting surfaces, the circulation at each panel is solved satisfying the no-penetration boundary condition, equation (4), which here is written as

$$[AIC]\ \Gamma = -u_n \tag{11}$$

where $[AIC]$ is the aerodynamic influence coefficient matrix (which gives influence of one panel on another one), Γ is the vector of circulation at each panel, and u_n represents the normal component of total velocity at panel's control points due to free-stream, body elastic deformation, mutual influence between panels, influence of the wake and any other influence of velocity field, as the presence of the propeller slipstream.

The force evaluation is also based on equations (6) and (7). The wake can be modeled as free or prescribed, in terms of including or not the self-induced velocity. In order to estimate the viscous drag, the local lift coefficient, c_l, of each strip is calculated, including the effects of all panels, wakes and other possible interferences in the velocity flow-field. Then, the corresponding drag coefficient, c_d, is determined based on a polar table (obtained via, *e.g.*, XFOIL).

Using UVLM as the aerodynamic solver also enables the introduction of propeller models into the assembly. Currently UM/NAST implements a Lifting Line for the blades plus a Viscous Vortex Particle for the propeller slipstream in order to simulate the propeller influence on the flight dynamics [20]. Mutual influence of the lifting surfaces on the propeller and propeller on lifting surfaces is included. Also, a structural representation of the rotating blades is incorporated in order to account for the gyroscopic effects.

As the structural model employs a 1D finite element representation and the UVLM uses 3D planar grid, an interface between both solvers is applied in order to transfer loads and displacements. Such mapping is based on the assumption of rigid behavior in the chordwise direction and on the principle of equivalence of virtual work between the forces at panels and forces transferred to beams.

As one of the goals in this work is the verification exercise of the different codes, the authors opted by not including propeller effects, nor viscous drag estimation. Also, for the UM/NAST simulations presented next, the implicit trapezoidal scheme was applied. As in the case of SHARPy, the wake is convected with just onflow velocity (accounting for body motion and gust), and wake-self induced velocity is not considered, reducing computational cost while still capturing information for the surface and wake interactions.

More details about the numerical parameters used in the simulations are provided in the following section.

3 NUMERICAL STUDIES

3.1 X-HALE configuration definition

The X-HALE features a number of challenging features for aeroelastic modeling and simulation. Firstly, it has a relatively complex geometry with multiple intersecting lifting

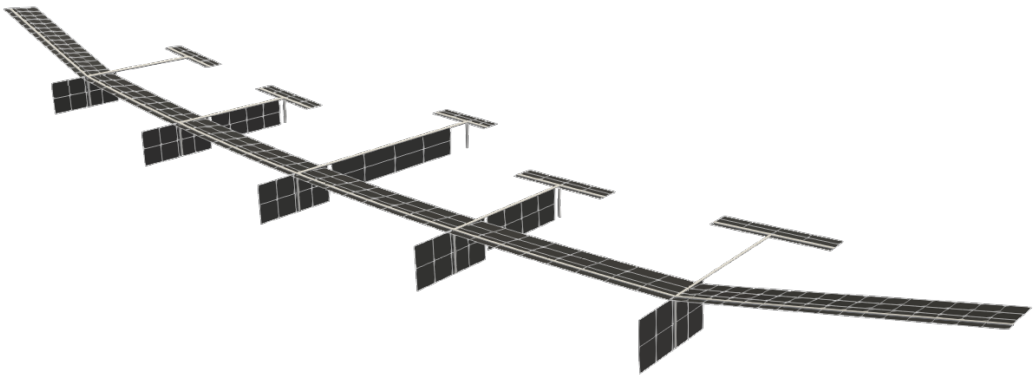

Figure 3: Aeroelastic model for the X-HALE used in this paper.

surfaces. Secondly, all its primary subcomponents are very lightweight and their flexibility need to be considered, which is done here with beam elements with elastic and inertia coupling. Thirdly, as wings are span-loaded, it has a rather involved mass distribution. The validation effort between both solvers requires generation of detailed models as similar as possible amongst them. Due to the different design philosophies, discretization, and numerical methods in the solvers employed, this is far from a trivial exercise. The structural, aerodynamic and aeroelastic results from this exercise are shown in this section.

The first bending mode of the aircraft has a natural frequency close to 0.60 Hz, which results in a strong coupling between the elastic and the flight dynamic modes. The relatively low stiffness in torsion of the main wing presents another set of challenges. The influence of the properties of the tails and their trim angle is more remarkable than for standard configurations, as they also affect the lift distribution of the wing by modifying its twist. It is also worth noting that being the tail in the wake of the main wing, the wake modeling is of relevance, specially in dynamic simulations [21].

Another feature that needs to be considered is the rotating central tail, as it modifies the stability properties of the platform. The results presented in section 3.3.2 show how an unstable dutch roll mode appears when the tail is horizontal, but does not with the vertical tail.

The fact that UM/NAST and SHARPy have evolved independently with the same target in mind means that while the approaches and methods are similar, their implementation details and numerical behaviour are not. As it will be seen, while static results have proven to be relatively unaffected past a certain level of refinement, this is not the case for the dynamic solutions.

Based on the studies performed by the authors it was evident that, depending on the kind of simulation considered and due to differences in some of the approaches used by each code (*e.g.* strain based vs. displacement based, weak vs. fully coupled FSI solution, integration scheme) the codes may require different spatial and temporal discretization to reach convergence. As will be presented next, the static and vertical gust simulations show a very good agreement between the two codes. However, the lateral gust simulations

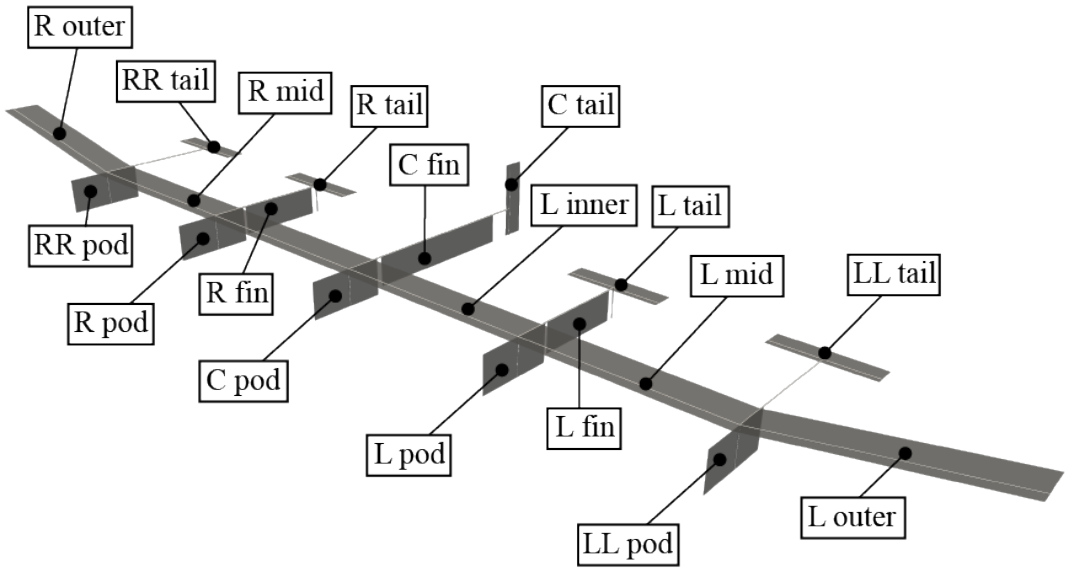

Figure 4: Nomenclature followed in the model description

showed a higher sensitivity in terms of the discretization, with the wing chordwise discretization affecting more the lateral DoF quantities and the wing spanwise discretization showing a higher effect for the vertical DoF quantities. Due to the complexity of the model and the number of parameters involved, a more detailed investigation about the convergence process for each code could not be performed and this will be addressed in future studies.

In SHARPy, the aerodynamic and structural models cannot be completely detached. In order to simplify the force mapping process between the different solvers, the VLM grid is required to be matching with the beam model. This means that the spanwise distribution of panels is the same as the structural nodes discretization. Because quadratic beam elements are used in SHARPy, two aerodynamic panels are required per beam element.

The stiffness distribution of the X-HALE model is given in Table 1 and based on the nomenclature indicated in Figure 4. For briefness sake, only right wing information is given, but the whole model is easy to reconstruct considering that the stiffness and distributed mass data in Table 2 are symmetrical. It is important to note that in that table, the mass for the pods is set at 10^{-8} kg/m. However, this is set this way because the whole mass contribution of the pod comes from the lumped masses. The lumped masses for every pod are given in Table 3, next, the aerodynamic model geometry is given in Table 4, and its discretization is shown in Table 5. It is important to note that in this table, N is the number of spanwise panels, and M is the number of chordwise panels. Lastly, the wake length is set at 4 meters, independently of the chordwise discretization.

Given that the trim shape can be significantly different to the jig shape, or even while flying in different conditions, stability and gust response needs to be assessed at every trim point of interest. We will consequently first investigate static aeroelastic equilibrium using both solvers.

Table 1: Stiffness data for X-HALE model.

Section [-]	EA [Nm^2]	GJ [Nm^2]	EI_y [Nm^2]	EI_z [Nm^2]	k_{14} (axial-IP) [Nm^2]	k_{34} (OOP-IP) [Nm^2]
R inner	2.14×10^6	5.93×10^1	1.12×10^2	6.35×10^3	0	4.63×10^1
R mid	2.14×10^6	5.93×10^1	1.12×10^2	6.35×10^3	0	4.63×10^1
R outer	2.14×10^6	5.93×10^1	1.12×10^2	6.35×10^3	0	4.63×10^1
fuselage	5.39×10^7	5.39×10^7	5.39×10^7	5.39×10^7	0	0
tail	3.21×10^6	2.14×10^1	9.10×10^1	4.27×10^3	7.44×10^4	2.26×10^-6
fin	5.39×10^7	5.39×10^7	5.39×10^7	5.39×10^7	0	0

Table 2: Distributed mass of the X-HALE model.

Section [-]	Mass [kg/m]	I_{xx} [kgm]	I_{yy} [kgm]	I_{zz} [kgm]	I_{yz} [kgm]	x_{cg} [m]	y_{cg} [m]	z_{cg} [m]
R inner	3.94×10^{-1}	8.1×10^{-4}	1.22×10^{-5}	7.97×10^{-4}	6.5×10^{-6}	0	2.94×10^{-2}	0
R mid	3.94×10^{-1}	8.1×10^{-4}	1.22×10^{-5}	7.97×10^{-4}	6.5×10^{-6}	0	2.94×10^{-2}	0
R outer	5.0×10^{-1}	8.1×10^{-4}	1.22×10^{-5}	7.97×10^{-4}	6.5×10^{-6}	0	2.14×10^{-2}	0
fuselage	0.0429	2.91×10^{-9}	1.46×10^{-9}	1.46×10^{-9}	0	0	0	0
tail	0.2614	1.6×10^{-4}	2.910×10^{-6}	1.57×10^{-4}	0	0	0.0144	0
pod	1×10^{-8}	2×10^{-8}	1×10^{-8}	1×10^{-8}	0	0	0	0
C fin	0.5092	3.19×10^{-3}	9.34×10^{-5}	3.28×10^{-3}	0	0	0	0
L/R fin	0.3208	8.17×10^{-4}	5.88×10^{-5}	8.76×10^{-4}	0	0	0	0

3.2 Static results

Static simulations have been performed in order to compare both aircraft model details and numerical methods. First, the structural and aerodynamic solvers are independently compared, before the full aeroelastic trim equilibrium of the aircraft is sought.

3.2.1 Structural cases

The structural cases are 1) gravity forces; 2) a vertical follower force, and 3) an out-of-plane bending follower moment at the wing tip. They are all applied on half a X-HALE vehicle clamped at the wing midpoint. These cases have been chosen to validate several aspects of the solver: the geometrical nonlinearity treatment, the follower forces and moment implementation and the gravity and stiffness distributions of the model.

Figure 5 shows the wing spar in-plane and out-of-plane displacements in a gravity-only loading case. For the sake of clarity only the wing spar position is shown, even though the case includes all the structural model of the aircraft.

Next, the half-aircraft model is subject, first, to a wing tip vertical follower force ($F_z = 15$ N) and, second, to a wing tip out-of-plane bending moment ($M_y = 30$ Nm). Follower-force effects are critical nonlinearities in aeroelasticity with large deformations, as the final orientation of the aerodynamic loads depends on the beam displacements and rotations at the equilibrium point. The wing spar nodal positions for both load cases and solvers are presented in Figure 6. A relative deflection of about 35% of the semispan is reached with the given forces. As it can be seen, excellent comparison is obtained between both structural solvers even under such extreme loading conditions.

Lastly, the structural modes and natural frequencies of the aeroelastically trimmed struc-

Table 3: Lumped mass data. Relative positions are given with respect to the pod/wing spar intersection node. Frame of reference: x right wing, y upstream, z up.

Mass [kg]	x_{cg} [m]	y_{cg} [m]	z_{cg} [m]	I_{xx} [kgm^2]	I_{xy} [kgm^2]	I_{xz} [kgm^2]	I_{yy} [kgm^2]	I_{yz} [kgm^2]	I_{zz} [kgm^2]
C pod									
0.3746	0	0.1	0	1.15×10^{-3}	0	0	8.90×10^{-4}	0	8.90×10^{-4}
1.0462	3.97×10^{-3}	0.0612	-0.0168	1.48×10^{-2}	2.32×10^{-4}	2.27×10^{-5}	2.82×10^{-3}	4.50×10^{-4}	2.50×10^{-4}
0.023	0	0.260	-0.023	0	0	0	0	0	0
L pod									
0.548	-0.01	0.090	0	1.54×10^{-3}	0	0	8.90×10^{-4}	0	8.90×10^{-4}
0.929	2.14×10^{-3}	0.04	-1.39×10^{-2}	1.13×10^{-2}	-1.21×10^{-3}	1.06×10^{-5}	3.21×10^{-3}	4.60×10^{-5}	8.48×10^{-3}
0.023	0	0.259	-0.023	0	0	0	0	0	0
R pod									
0.548	-0.01	0.090	0	1.54×10^{-3}	0	0	8.90×10^{-4}	0	8.90×10^{-4}
0.929	2.14×10^{-3}	0.04	1.39×10^{-2}	1.13×10^{-2}	-1.21×10^{-3}	1.06×10^{-5}	3.21×10^{-3}	4.60×10^{-5}	8.48×10^{-3}
0.023	0	0.259	-0.023	0	0	0	0	0	0
LL pod									
0.571	-0.01	0.091	0	1.54×10^{-3}	0	0	8.90×10^{-4}	0	8.90×10^{-4}
0.929	2.14×10^{-3}	0.04	-1.39×10^{-2}	1.13×10^{-2}	-1.21×10^{-3}	1.06×10^{-5}	3.21×10^{-3}	4.60×10^{-5}	8.48×10^{-3}
0.023	0	0.259	-0.023	0	0	0	0	0	0
RR pod									
0.571	-0.01	0.091	0	1.54×10^{-3}	0	0	8.90×10^{-4}	0	8.90×10^{-4}
0.929	2.14×10^{-3}	0.04	-1.39×10^{-2}	1.13×10^{-2}	-1.21×10^{-3}	1.06×10^{-5}	3.21×10^{-3}	4.60×10^{-5}	8.48×10^{-3}
0.023	0	0.259	-0.023	0	0	0	0	0	0

Table 4: X-HALE aerodynamic model description.

Part	Span	Chord	E. Axis	Dihedral	Airfoil
[-]	[m]	[m]	[% chord]	[deg]	[-]
inner/mid	1	0.2	28.8	0	EMX-07
outer	1	0.2	28.8	10	EMX-07
C tail	0.385	0.11	32.35	0	FLAT
LL/L/R/RR tail	0.48	0.11	32.35	0	FLAT
C fin	0.15	0.78	122.56	0	FLAT
L/C/R pod	0.184	0.38	60.93	0	FLAT

ture have been extracted with both codes. The results up to the tenth mode are presented in Table 6.

3.2.2 Aerodynamic cases

The total aerodynamic forces in wind-oriented frame of reference have been calculated for the underformed main wing. In order to assess the VLM results isolated from the aeroelastic effects and the sensitivity with the inclusion of non-symmetrical airfoil, the resultant forces for a symmetric and the cambered airfoil EMX-07 (Fig. 7) in the main wing are calculated. As an external reference, the same geometry has been simulated in TORNADO [22], which is an open-source steady vortex-lattice solver with a horseshoe wake. The distribution of aerodynamic forces plays a very important role in the final aeroelastically trimmed shape. Studies in this work have shown a strong sensitivity of the distributed aerodynamic forces and beam deflections in aeroelastic equilibrium with changes in the camber line. Therefore, special care must be taken when calculating and discretizing the camber line from the airfoil coordinates when performing nonlinear aeroelastic analysis using lifting surface models. In the studies conducted by the authors, it has been determined that for static simulations with X-HALE, 8 or more chordwise panels distributed uniformly replicate the camber line satisfactorily.

Table 5: Aerodynamic grid discretization

Part	SHARPy All cases		UM/NAST Static and Long.		UM/NAST Lateral	
[-]	M	N	M	N	M	N
inner/mid	8	8	8	12	12	30
outer	8	16	8	12	12	30
C tail	3	4	8	6	8	6
LL/L/R/RR tail	3	4	8	6	8	6
C fin	4	2	8	2	8	2
L/C/R pod	4	2	8	2	8	2

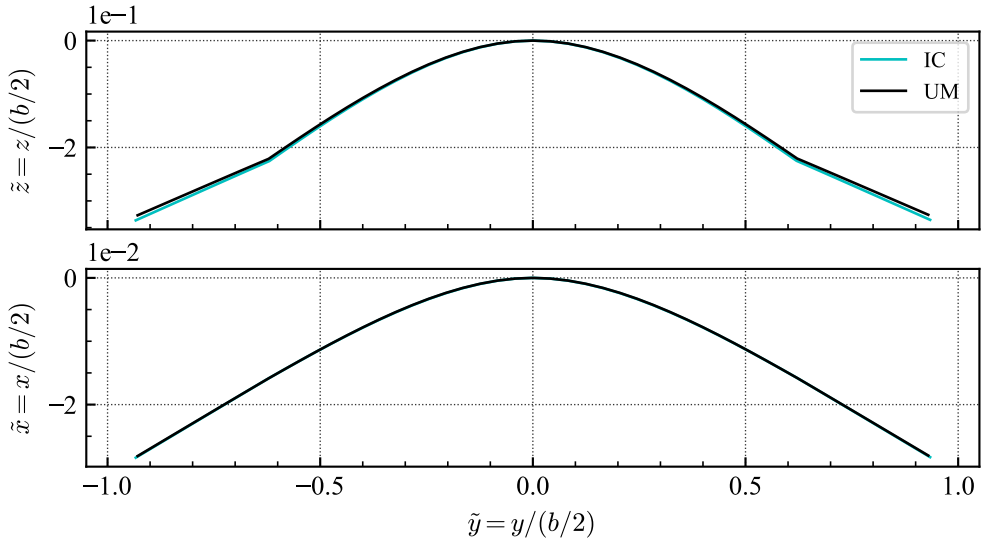

Figure 5: Spar deformation when subject to gravity.

Table 7 shows the total aerodynamic forces in wind axes for a wing angle of attack $\alpha = 4°$, and Table 8 shows the flight conditions used for the results presented in this paper. Induced rag prediction in VLM codes is more difficult to achieve than lift due to its quadratic dependency. Due to the potential nature of the VLM, no viscous drag information can be obtained without additional information such as Reynolds number-dependant C_D *vs* C_L databases obtained through experimental or numerical methods or other empirical laws. It has been decided to avoid adding more drag contributions as they would add another layer of uncertainty requiring separate analysis and validation. In sight of the sensitivity of the results with the camber line input, the results shown in Table 7 are considered to be similar enough to move onto the static aeroelastic simulations.

3.2.3 Aeroelastic cases

The aeroelastic cases presented in this section are of two kinds. The first is a comparison of the structural deformations at a given flight condition for both codes while the second is a comparison of the trim conditions calculated with each code.

The aeroelastic deformation comparison given a flight condition has been run for three different body angles of attack: 0, 3 and 5 degrees. It is important to note that the body angle of attack is the angle between the free stream and the undeformed central fuselage, as the main wing presents a structural twist of 5 degrees. In addition, the thrust has been

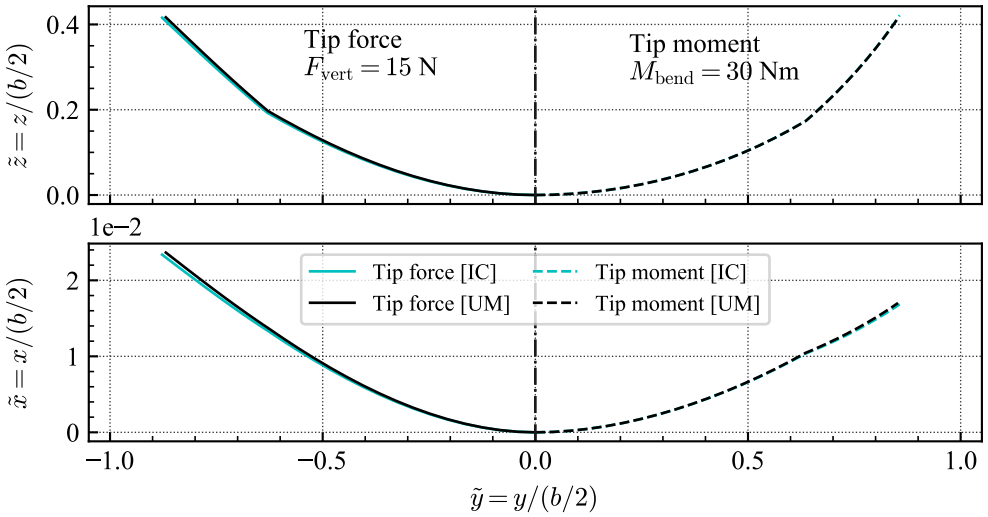

Figure 6: Spar nodal positions under a follower force ($\tilde{y} < 0$) and moment ($\tilde{y} > 0$).

Table 6: Structural natural frequencies (in Hz) of the aeroelastically trimmed X-HALE structural model.

Modes	Mode type	Freq. - IC	Freq. - UM
1 & 2	Out of plane I	0.57	0.59
3 & 4	Torsion I	2.50	2.57
5 & 6	Out of plane II	3.62	3.70
7 & 8	In plane I	4.58	4.45
9 & 10	Torsion II	6.59	6.57

set to zero and the tails are aligned with the fuselage ($\delta = 0°$). The aircraft is assumed to be clamped on the central fuselage-main spar intersection. Results are shown in Figure 8. From it, one can see that even in deflections larger than 20% of the semi wing span, the difference in wing deformation between both solvers is almost negligible, showing again their suitability for this problem.

Trimming a very flexible aircraft is potentially more complex than a rigid one. In addition, the unconventional configuration of the X-HALE contributes to this difficulty. Given the relatively low torsional stiffness of the wing spar, the effect of the multiple tails is not straightforward: an increase in control surface deflection ($\delta > 0$) has two effects. First, a nose-down pitching moment and a momentary contribution towards increasing the overall lift; and second, a loss of lift in the main wing, specially in the outer parts of the wing due to a torsion load that reduces the effective twist.

X-HALE has some characteristics that, if considered in the trim routine, can simplify the analysis. First, the four outer tails are actuated using a single input. That means that a single "tail deflection" parameter can be used. Second, the five motors are controlled using a *symmetric* and *antisymmetric* thrust in order to provide lateral control. Given that the only not symmetric contribution comes from the mass distribution, and the centre of gravity is deviated less than 4 mm from the longitudinal axis, trim is sought using the longitudinal equations only. The residual forces and moments in the lateral equations after trim are all the same order of magnitude (or lower) than the trim tolerances, and consequently, the *antisymmetric* component of the thrust vector is set to zero in forward flight conditions.

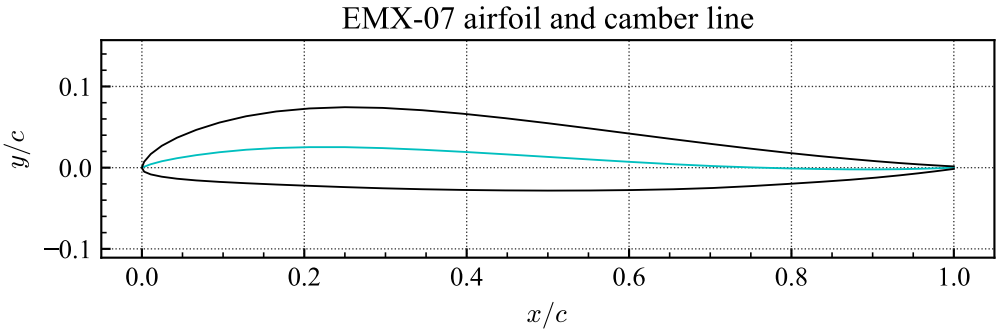

Figure 7: EMX-07 airfoil used in main wing.

Table 7: Aerodynamic forces (in N) on the rigid aircraft, $\alpha = 4°$.

Code	Airfoil	Induced Drag	Lift
IC-SHARPy	NACA 0012	0.28	58.60
	EMX-07	0.33	63.61
UM-NAST	NACA 0012	0.29	61.69
	EMX-07	0.32	64.00
TORNADO	NACA 0012	0.28	58.80
	EMX-07	0.31	61.46

In order to enforce straight and steady unperturbed flight in relatively long dynamic simulations, the total residuals from the trim routine are still applied (with opposite sign) at the wing spar centre as a follower force.It is important to note however that applying those small constant balancing loads will not affect the vehicle dynamics, which is governed by loads variations from the equilibrium condition.

Typical trim algorithms assume constant aerodynamic derivatives in a certain domain around the trimmed condition [23]. This is not necessarily valid in the case of flexible aircraft: the domain around which this hypothesis stands will be most probably reduced. Aerodynamic surfaces can morph based on factors that vary during the trim routine, such as tail-induced wing twist or lift distribution variations due to structural deformations. Two approaches can be followed to tackle this: aerodynamic derivatives can be updated using numerical methods every iteration, or they can be assumed constant and expect the optimisation method to converge nevertheless. The approach implemented in SHARPy is based on a modified Newton-Raphson, where an approximated diagonal Jacobian is updated at every iteration using first-order finite differences with the values taken from previous iterations. Lastly, the objective function to assess convergence is the 2-norm of the longitudinal resultants vector.

In UM/NAST, a method based on Newton-Raphson is also employed for the trim. However, instead of numerically recalculate the Jacobian matrix at each step (by applying state perturbations), which is an expensive operation, the Jacobian is calculated just in the first step and then updated on the next iterations by using Broyden's method [24]. This reduces significantly the computational cost of the trim. For the objective function, both longitudinal trim (considering just the loads acting in the longitudinal plane), as well as lateral trim (considering all the 6 resultant loads acting on the aircraft) can be performed, just requiring an adequate number of trim parameters to be defined. Those resultant loads are calculated at the origin of the aircraft, which is modeled as clamped

Table 8: Flight conditions used in this paper.

	Value
Free stream velocity, U_∞	14 [m/s]
Density, ρ_∞	1.225 [kg/m^3]
Gravity acceleration, g	9.807 [m/s^2]

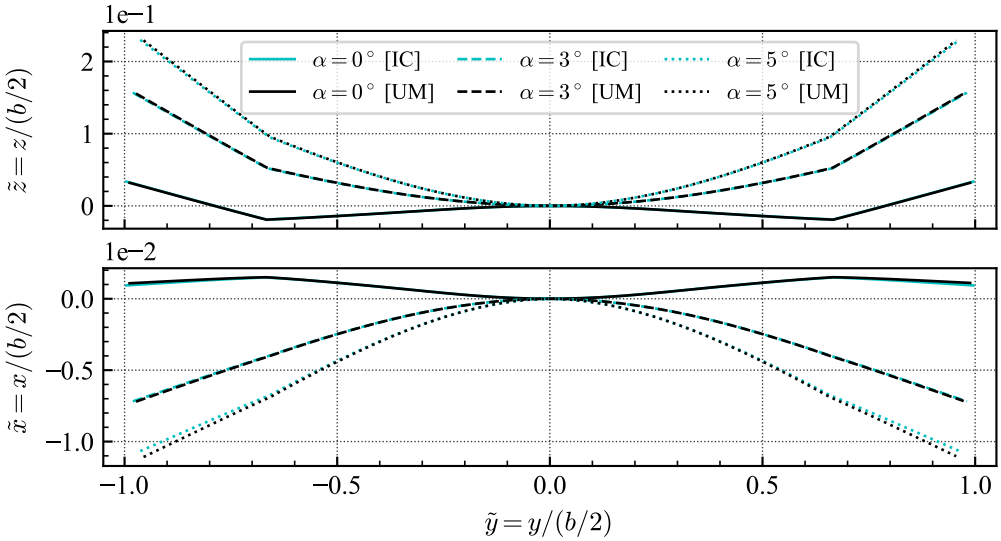

Figure 8: Spar deformation for different angles of attack

and they should be smaller than a user-defined tolerance in order for the trim parameters to be determined. In this work, as previously stated, the longitudinal trim was calculated.

The computed trim conditions for both the vertical and horizontal central tail orientations are presented in Table 9. The agreement for α and δ between codes is good, while the thrust reflects the difference in drag prediction. Further work will address the discrepancy in drag prediction between codes.

Table 9: Trim results for cruise flight

Code	Tail orientation	α [°]	δ [°]	T [N]
IC-SHARPy	Vertical	2.64	1.19	0.223
	Horizontal	2.21	0.52	0.213
UM-NAST	Vertical	2.59	1.15	0.179
	Horizontal	2.38	0.66	0.179

3.3 Gust response

The open-loop response of the X-HALE is simulated with SHARPy and UM/NAST and compared on deterministic "1-cos" gust profiles. Both lateral and vertical gusts are addressed with the aim of identifying the main features of the aeroelastic response of the platform in longitudinal and lateral directions. For this work, gusts are sized such as the instantaneous angle of incidence of any section of the aircraft is in the aerodynamic linear range at any moment. This is to avoid having to introduce stall correction models in the studies. Lastly, the response of the aircraft with its central tail in vertical or horizontal position are assessed.

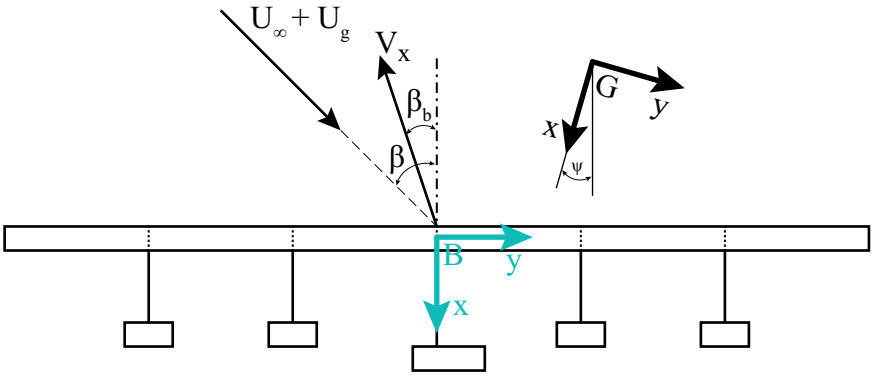

Figure 9: Inertial (G) and body-attached (B) frames of reference definition.

In order to evaluate the response of the aircraft to the deterministic gust profiles, trajectory, attitude angles, wing root loads and wing tip deflection are recorded. All results shown here are given in inertial, G (x downstream, y right, z up), or body-attached, B (x aft, y right wing tip, z local vertical upwards) frame of reference. It is important to note then, that the plane is flying towards a negative x and consequently, an increase in forward speed translates in $\Delta V_x < 0$ in both frames of reference.

An array of different gusts has been defined and the response of the X-HALE with vertical and horizontal central tail has been simulated. First, a vertical "1-cos" gust has been run in order to have a first glimpse at the X-HALE response with both codes. Next, a set of different length lateral "1-cos" gusts are run. The analysis has been simplified by setting the gust reference velocity ($\bar{U}_g$) to 15% of the free stream speed. It has been chosen so that the vertical surfaces will only operate in the linear regime, as the instantaneous sideslip angle is $\beta_g = \arctan\left(0.15U_\infty/U_\infty\right) = 8.53°$. The deterministic "1-cos" velocity profile is given as

$$U_g = \frac{\bar{U}_g}{2}\left(1 - \cos\left(\frac{x - x_{\text{offset}}}{H}\pi\right)\right) \; ; \qquad \text{if } -2H < x - x_{\text{offset}} < 0 \tag{12}$$

where H is the gradient of the gust, that is, the distance required to reach the reference velocity and x_{offset} is the initial position of the gust front with respect to the aircraft main spar.

Given the number of lifting surfaces and their different locations, it is important to know when the gust is reaching each of the different tails and fins. Figure 10 presents the time history of the gust contribution to the incoming velocity for several lifting surfaces with relation to the reference axis of each surface, such as the main wing, the outer tails and the centre tail. In this plot, and in all the remaining ones, the time variable is nondimensionalized as

$$\tilde{t} = t \cdot U_\infty/(c/2). \tag{13}$$

This choice of a convective definition of the nondimensional time is a reflection of the focus of this paper in a short period after the gust, where structural response and flight dynamics are tightly coupled. The long-term effects of the gust, where the flight dynamics and the flight path in general can present significant deviations from the undisturbed case, are left for future work.

It is also important to note that all results presented here include an $x_{\text{offset}} = -1$ m (see

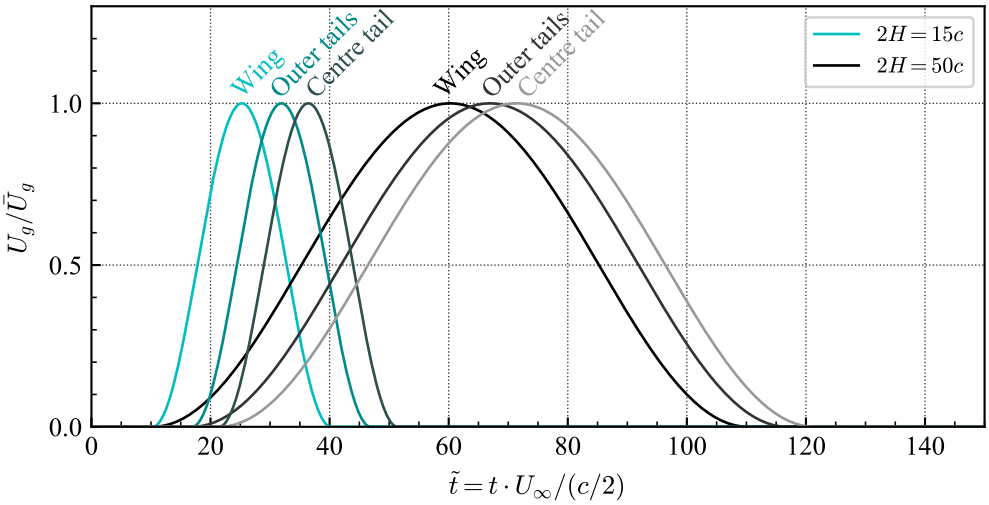

Figure 10: Gust velocity time histories for different aerodynamic surfaces (as seen from the elastic axis in steady forward flight).

equation (12)). The simulations have been run for 10 physical seconds, which equates to $\tilde{t}_{\max} = 1400$.

3.3.1 Vertical gust

A vertical "1-cos" gust has been run for the 2 different tail orientations. A single gust gradient and reference velocity combination has been run. The wing spar centre vertical trajectory is shown in Figure 11 for the vertical and horizontal configurations. It is easy to observe an oscillatory motion in the longitudinal plane. An interesting observation is that both codes agree that the period and amplitude of this mode is weakly dependent on the orientation of the central tail. Figure 12 shows the trajectory velocity in body frame

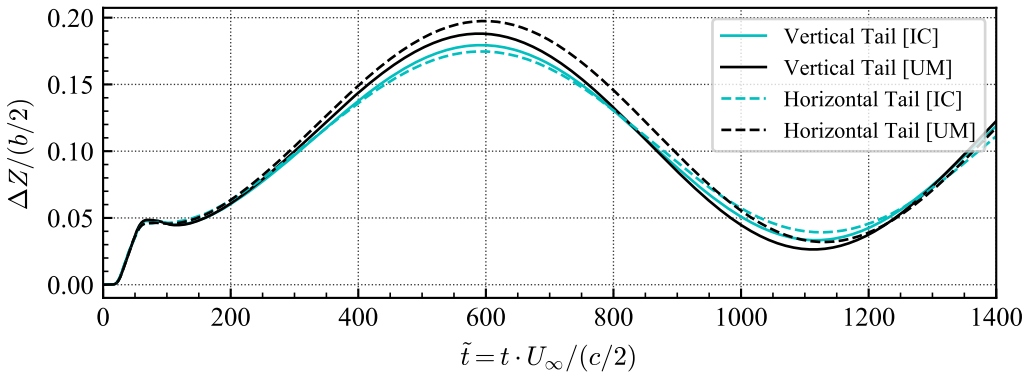

Figure 11: $2H = 15$ chords, vertical gust response: wing spar center trajectory.

of reference. The agreement between codes is good, specially in the transient phase of the response, which is more relevant for loads. The V_x component of the velocity (upper plot) presents a feature that will be present in the majority of results here shown. The results corresponding to the SHARPy code present a clearly lower structural damping. The oscillations in this case in V_x correspond to the in-plane bending oscillations of the wing that transmit to the wing root. This oscillation would not be found on the corresponding velocity component at the centre of gravity. However, given that for very flexible aircraft the centre of gravity position is dependant on the structural deformations, it has been

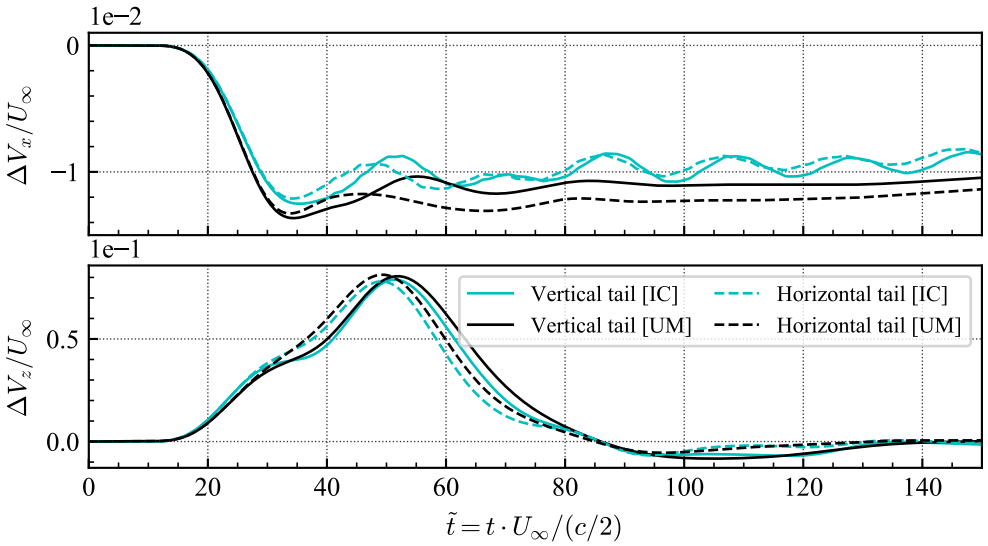

Figure 12: $2H = 15$ chords, vertical gust response: body velocity in body-attached frame of reference. Long simulation (10 s in physical time).

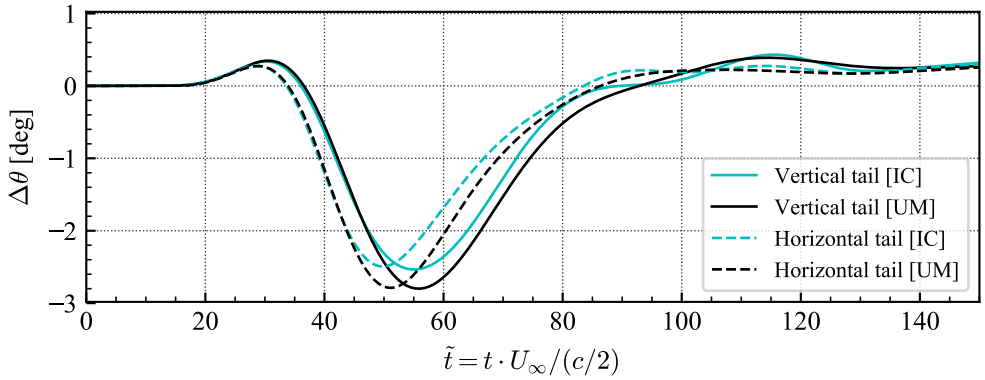

Figure 13: $2H = 15$ chords, vertical gust response: wing root pitch angle history.

decided to use a fixed point in body frame of reference. Figure 12 shows the rigid body velocity in body-attached (B) frame of reference and it is better understood together with the pitch angle increment history (Fig. 13). Figure 10 indicates that the outer tails enter the gust around $\tilde{t} \approx 20$ and reach the peak velocity at $\tilde{t} = 35$. This can be observed in Figure 13, where the pitch reaches a maximum due to the wing-only excess of lift and then the increasingly stronger tail influence causes it to pitch down heavily. The influence of the main wing in the pitch up part of the response is weaker than could be expected from conventional aircraft. This is due to the span-loading of the X-HALE, where the mass is distributed along the span, rather than the fuselage, like typical aircraft do. Because the main contribution to the lift and mass of the aircraft comes from the main wing, the aerodynamic centre and the centre of mass are located close to each other. Thus, a lift increment in the wing causes a vertical velocity increase, but not a strong pitch up tendency. The fact that the centre of lift and gravity are so closely located also affects the damping of the longitudinal motion.

The tail orientation also has an effect on the pitch down part of the response ($30 \lesssim \tilde{t} \lesssim 50$). The pitch peak value is similar for both tail orientations. In contrast, the peak is reached earlier in time for the horizontal tail. This is a predictable result, as the increased horizontal wet area in the aft part of the aircraft will make the aircraft pitching

characteristics more responsive to perturbations in α.

Other interesting feature of the longitudinal response is the lowly-damped phugoid motion. A rough approximation for the angular frequency and damping of the phugoid mode can be obtained from classic flight dynamics theory with a few other simplifications such as $V_z = \dot{V}_z = 0$ and $\alpha = 0$ (see [25]). The resulting expressions for the phugoid angular frequency, ω_n, and damping, ζ, are:

$$\omega_n = \sqrt{2}\frac{g}{U_0}, \quad \zeta = \frac{1}{\sqrt{2}}\frac{C_{D0}}{C_{L0}} \tag{14}$$

where $U_0 = U_\infty = 14$ m/s and C_{L0}/C_{D0} is the efficiency in cruise conditions. Substituting in the angular frequency equation, we obtain that the period for the phugoid given by this approximation is $T_{\text{phugoid}} = (\omega_n/(2\pi))^{-1} = 6.34$ s. The longitudinal oscillatory mode in Figure 11 has a period of 7.5 s. This is a reasonably good agreement in sight of the coarseness of the approximation leading to equation (14), where no centre of mass position, C_{mq} or $C_{m\dot{\alpha}}$ influence is considered, as the pitching-moment equation was not considered.

The approximation for the damping in equation (14) effectively states that the more efficient an aircraft is, the more undamped the phugoid mode. Given the high-aspect ratio of the X-HALE, its efficiency is high, and thus $C_{D0} \ll C_{L0}$. The resulting damping coefficient will be small in first approximation. Other simulations conducted by the authors show an influence of the central tail orientation in the damping of the motion. This behaviour cannot be seen with the analytical approximations here used, as the influence of the tail would be captured through C_{mq} and $C_{m\dot{\alpha}}$. The cases here shown have not been run long enough to extract a definite trend from the trajectory about the damping of the phugoid, but in sight of the first cycle, the horizontal tail case shows a first tendency to damp the motion quicker than the vertical tail one.

Lastly, the time history of the wing tip deformation for the early stages of the response is shown in Figure 14. Here, the SHARPy deformation history of the wing in the in-plane motion shows an oscillatory motion that could also be seen in the V_x component of the body velocity in Figure 12. We note that in-plane structural vibrations are challenging to determine accurately, specially when running potential-flow solvers, where the main contribution to in-plane force is the induced drag. The oscillations in this direction have an effect in the effective incoming speed of the flow, and this effect is much weaker than the out-of-plane equivalent, where aerodynamic damping plays a major role in the aeroelastic response. On the other hand, vertical displacements, which are an order of magnitude larger and directly affected by the input vertical gust, show an excellent agreement.

3.3.2 Lateral gust

Central tail orientation influence. One of the most remarkable features of the X-HALE configuration is its ability to modify its stability properties by flipping the central tail between vertical and horizontal positions. Flight tests [4] have shown that the aircraft is laterally unstable in open loop when the central tail is horizontal, while flipping it to the vertical position damps that unstable mode even after onset.

The results presented in this section show a difference in how the roll and yaw are coupled depending on the tail orientation (Fig. 16). When the tail is positioned vertically, the

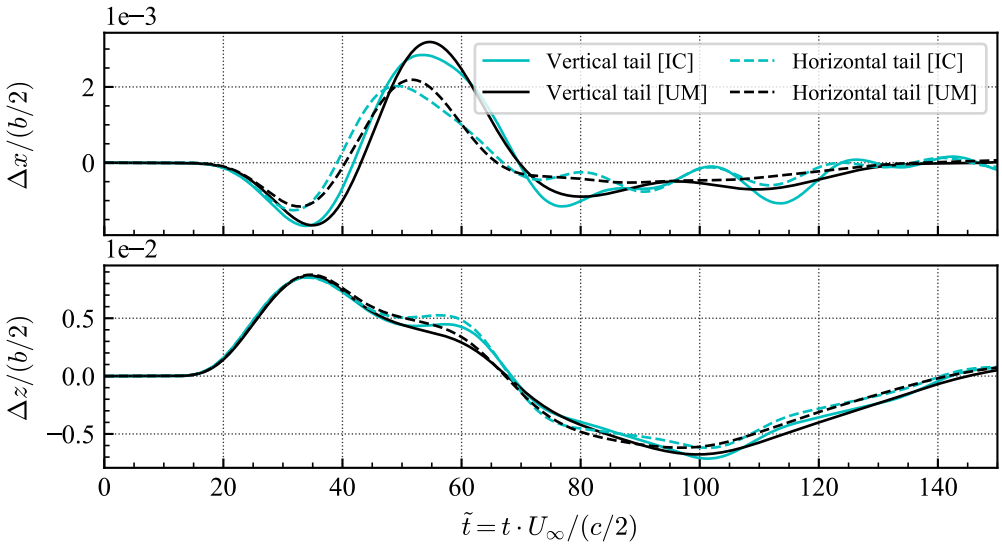

Figure 14: $2H = 15$ chords, vertical gust response: wing tip displacement in body-attached axes.

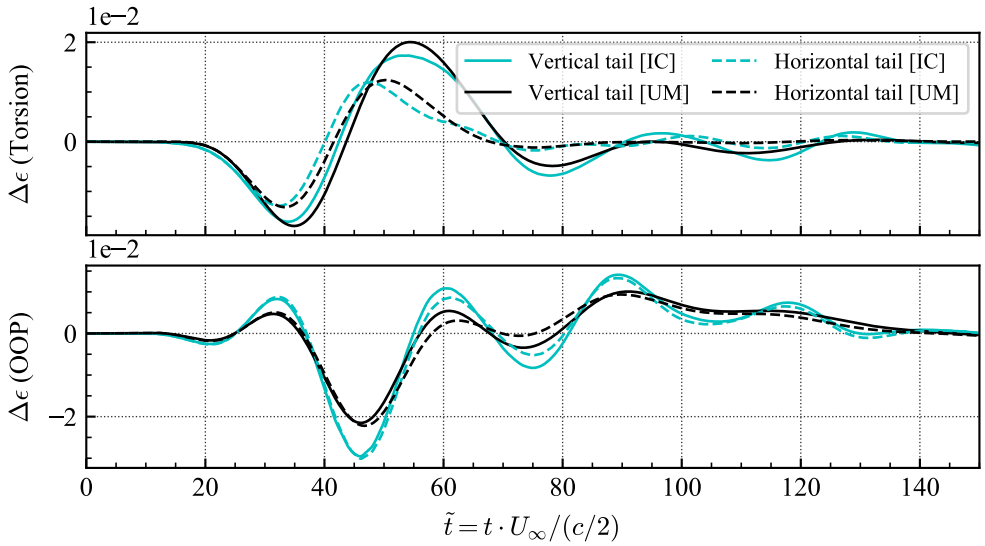

Figure 15: $2H = 15$ chords, vertical gust response: right wing root element strains.

instants where roll reaches 0° are the instants where the yaw reaches a local extremum. This behaviour is what would be expected of a conventional aircraft. In contrast, the tail position horizontally modifies the lateral behaviour of the aircraft. Local extremum of yaw are followed closely by a roll local extremum. This mode is known as dutch roll. Figure 17 isolates the coupling between roll and yaw for the two tail orientations. The vertical central tail case (left of the figure) shows a correlation between ϕ and $\mathrm{d}\psi/\mathrm{d}\tilde{t}$, where a positive roll (left wing down) is accompanied by a negative (yaw right) tendency due to adverse yaw effects. Adverse yaw appears in uncoordinated turns, where a roll input is not followed by a rudder input to yaw the aircraft towards the lower wing.

The right plot in Figure 17 shows a very different behaviour, where the maximum values in yaw time derivative are reached with zero roll. This can be understood as a "wiggling" motion of the tail which is the main characteristic of the dutch roll mode.

Figure 19 shows the time history of the crab angle β_b. This measures the angle between the longitudinal axis of the aircraft and its instantaneous velocity in body frame of reference.

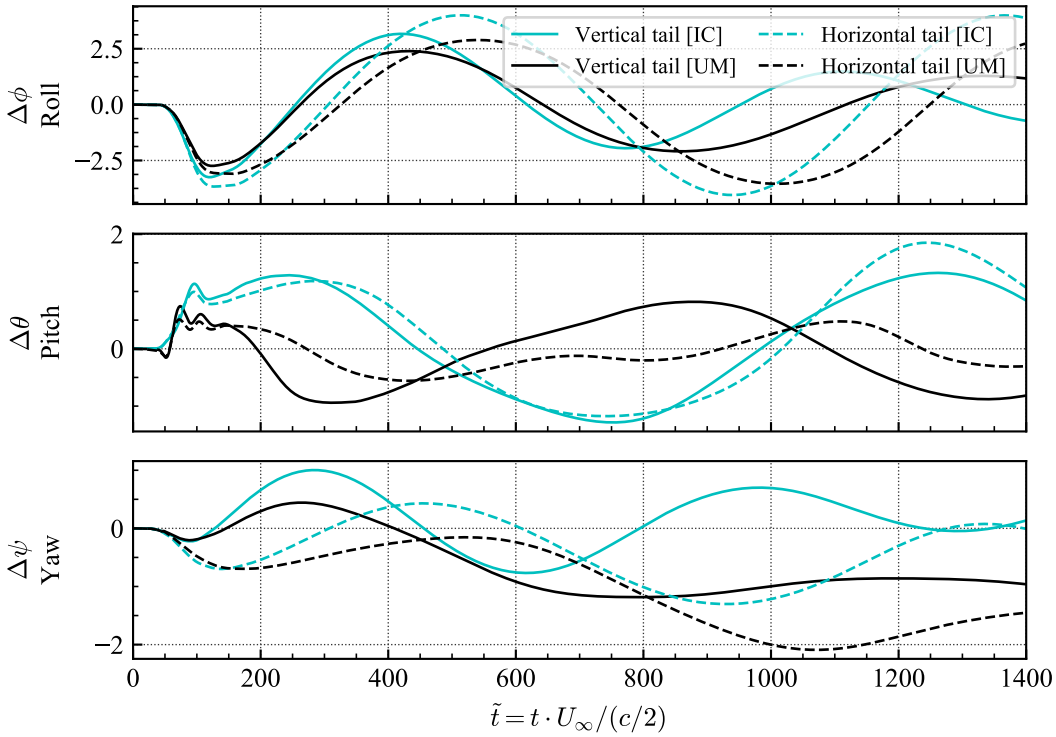

Figure 16: $2H = 50$ chords, lateral gust response: attitude angles (in degrees). Long simulation (10 s in phisical time).

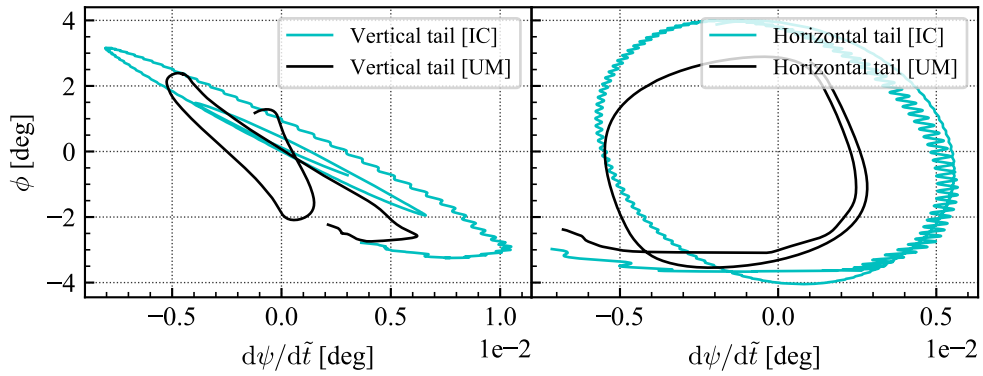

Figure 17: Influence of central tail configuration in the dutch roll mode. $2H = 50$ chords, lateral gust response: roll (ϕ) vs yaw (ψ) time derivative. $100 < \tilde{t} < 1400$.

Its definition is shown in Figure 9, and it is calculated as:

$$\beta_b = \arctan(V_y/V_x). \tag{15}$$

It is effectively a measure of the rigid body motion contribution to the sideslip and equates to the sideslip angle when no gust is actuating. It can be observed how the first peak value is lower in absolute value for the horizontal tail configuration. However, the damping of the vertical tail for the next cycle is visibly greater. This is consistent with the previous discussion about lateral stability. The horizontal tail presents an unstable flight dynamics mode caused by the lack of damping of sideslip excursions when coupled with a rolling motion.

Figure 18 shows the lateral rigid body velocity of the aircraft during and immediately after encountering the gust. Two distinct slopes can be seen: one before and one after

$\tilde{t} = 80$, when the gust reference velocity has already passed and the gust influence is decreasing (see Fig. 10). Due to the momentum acquired during the gust encounter, the aircraft keeps drifting to the right, even once the gust has passed, but it does so with a smaller lateral acceleration. The horizontal tail result has a smaller lateral velocity if

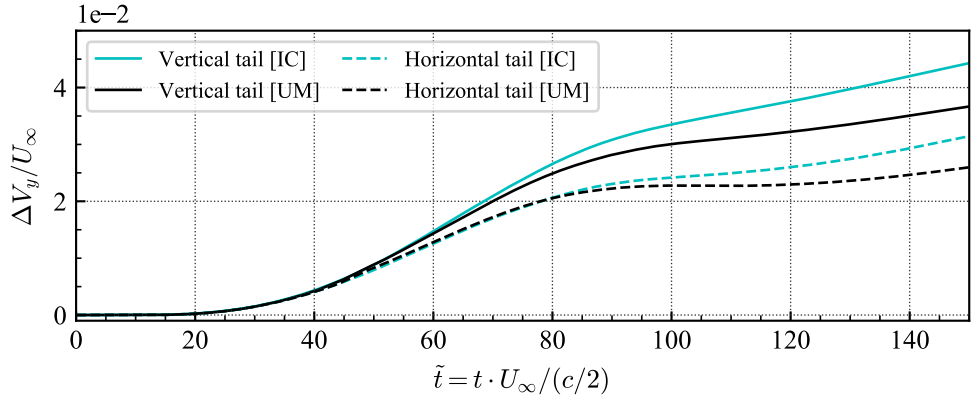

Figure 18: $2H = 50$ chords, lateral gust response: rigid body velocities in body-attached FoR.

compared to the vertical tail aircraft due to the reduced lateral area. The discrepancies that arise after approximately $\tilde{t} = 80$ are due to the different methods and discretizations in each code. It is interesting to see that details of discretization have a much stronger effect in lateral gust response computations that on the equivalent vertical gust.

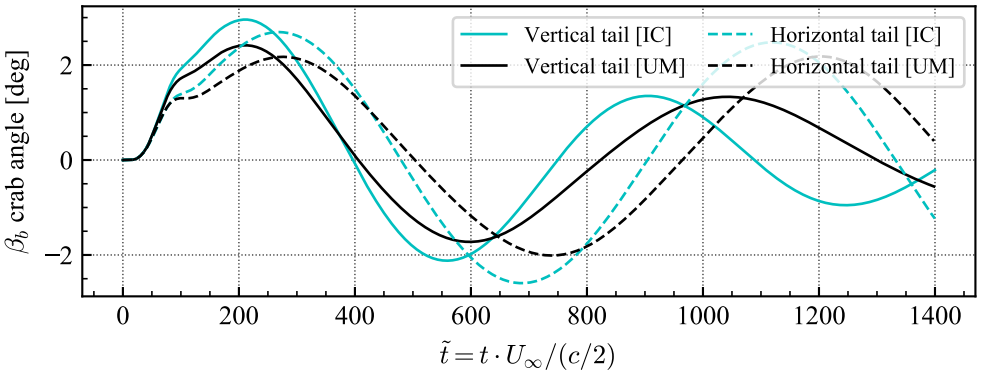

Figure 19: $2H = 50$ chords, lateral gust response: crab angle.

Lastly, the right wing torsional and out-of-plane bending strains are shown in Figure 20. The fact that strains are affected by potentially every aspect of the simulation, from aerodynamic loads, stiffness effects until inertial effects, makes them a challenging quantity to compare between codes. The discrepancies in the vertical flight dynamics due to the discretization and methods probably have an important effect in the wing root strains.

Gust length influence. When considering the gust response of a very flexible aircraft, the linearity of the response cannot be assumed in the first place. The rigid body couplings with the structural dynamics result in potentially complex behaviour. Due to this, the same cases shown in the previous section have been run with a gust gradient of 7.5 chords (or 1.5 m), instead of the original 25 chords (5 m). From a structural point of view, we can expect the response to be similar as long as the excitation is approximately in the same range of frequencies. For example, the $2H = 50c$ gust has an excitation frequency of $f_{50c} = 1.4Hz$ ($f = (2H/U_\infty)^{-1}$). Going back to Table 6, it can be seen that 1.4 Hz

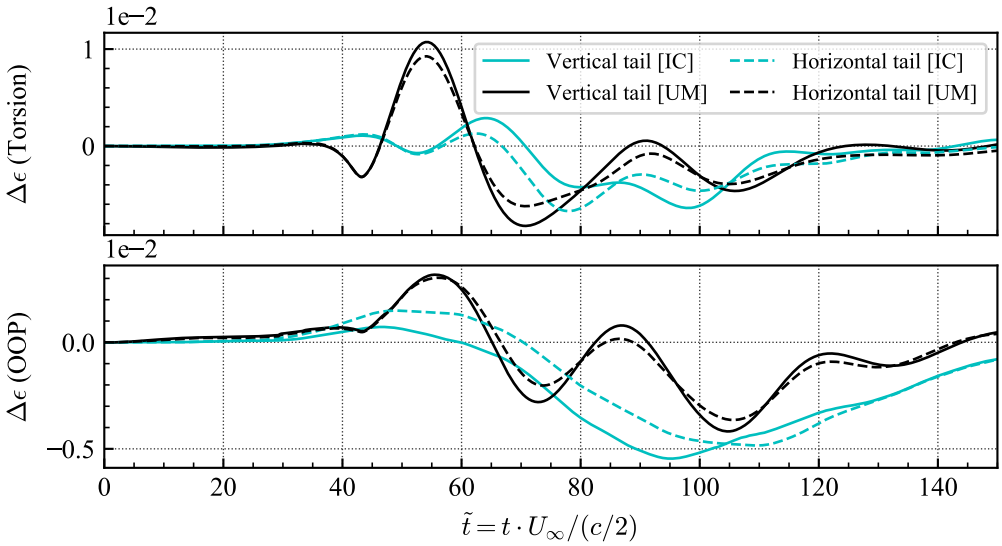

Figure 20: $2H = 50$ chords, lateral gust response: right wing root element strains.

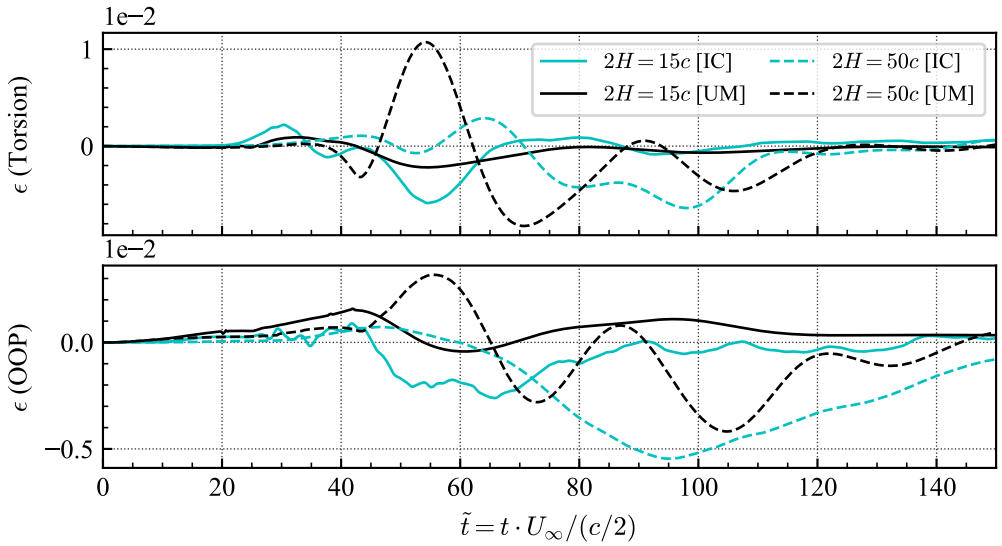

Figure 21: Lateral gust response with vertical tail: right wing root strains.

falls between the Out of Plane I and Torsion I modes. However, the shorter $2H = 15c$ gust gives an excitation frequency of $f_{15c} = 4.67$ Hz, which now will be very close to the In Plane I mode, and relatively close to Torsion II. From this, it is easy to infer that, while the flight dynamics response might be similar between the two gust lengths, the structural response will most likely be different.

Figure 21 presents the right wing root strain for both gust lengths. More visible in the UM/NAST results than the SHARPy ones, there is an in-phase interaction between the out-of-plane and torsion strains for the $2H = 50c$ gust. The $2H = 15c$ gust presents a different behavior, with a weaker coupling between the two strains.

On the other hand, the frequency of the V_y oscillations (Fig. 22) presents a dependency on the gust length input. During the first cycles of the V_y oscillations, the response is characterized by its higher frequency for the $2H = 50c$ gust than the shorter $15c$ one. The excitation mechanism between the two gusts differs substantially due to the relative length of the gust with respect to the longitudinal dimension of the aircraft. Given that

X-HALE measures approximately 1.4 meters long, the "1-cos" shape of the gust will affect how it affects the aircraft resultant forces and moments. The short gust has a gradient (H) comparable to the aircraft length, while the longer one is three times longer than X-HALE. That means that in the short gust case, the aerodynamic surfaces will be affected in sequence as the aircraft flies through it, while in the longer gust, the excitation will be more similar to a quasi steady increase in sideslip angle.

The two gusts then excite different flight dynamics mechanisms. The longer gust response is closer to the pure flight dynamics mode frequency, while the shorter gust presents a more complex interaction and will potentially decay with time towards a pure flight dynamics mode.

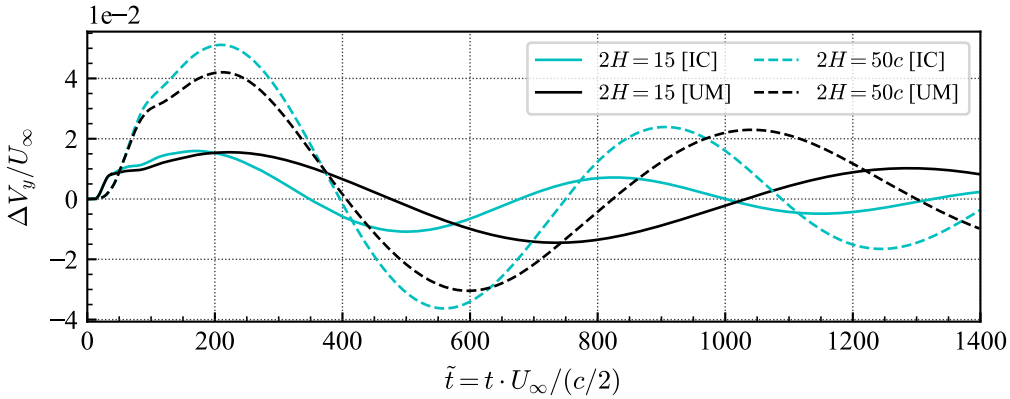

Figure 22: Lateral gust response with vertical tail: lateral rigid body velocity in body-attached frame of reference

This idea is backed by the fact that the unstable dutch roll mode discussed in the former section is excited in a more efficient way with the $2H = 50c$ gust, rather than the shorter version. Being the dutch roll an identifiable flight mode, the lower-frequency (but short enough in comparison with the flight dynamics frequencies), simpler, closer to quasi-steady excitation of the 50 chords gust destabilizes the aircraft faster than the shorter, more complex input. Figure 23 shows the right wing root strains time history for the full $\tilde{t} = 1400,\ t = 10$ s simulations. While the structural response of the aircraft after the short gust –in continuous lines– is damped quickly, the discontinuous line of the longer gust shows the interaction of the growing dutch roll mode with the aircraft structure in an also growing trend.

4 CONCLUDING REMARKS

Given the lack of insight and official certification guidelines for the design of a very flexible aircraft subject to lateral gust, this work had the goal of provide useful analysis towards that gap, providing also insight for the simulation's requirements for this complex non-linear response scenario. For this, the X-HALE, an aeroelastically representative model of a High-Altitude, Long-Endurance aircraft has been modeled. In order to verify the numerical results, and in view of the insufficient experimental data for validation, a detailed code-to-code comparison for two independent nonlinear aeroelasticity frameworks from Imperial College London and the University of Michigan was first performed. This comparison involved an extensive array of verification cases including structural, aerodynamic and aeroelastic static simulations. Finally, gust response to vertical and lateral

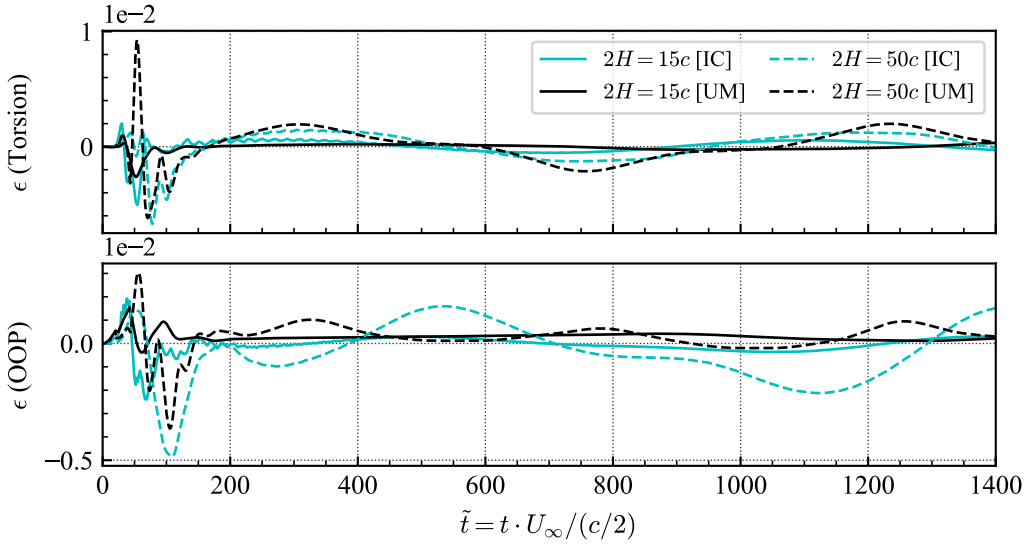

Figure 23: Lateral gust response with horizontal tail: right wing root strains full time history.

excitations were analyzed, with a special focus on the effects of central tail orientation and gust length on the very flexible aircraft response.

The X-HALE configuration presents a set of characteristics not common in conventional aircraft, but potentially similar to other HALE configurations, such a span-loaded configuration with distributed payloads along the wing, a low stiffness in torsion and out-of-plane bending, and an unconventional geometry, with 5 tails distributed along the span.

Despite the different approaches and methods implemented in the codes and the complexity of the model, the validation exercises show excellent agreement for both structural and aeroelastic static cases. A discussion on trim procedures for nonlinear flexible aircraft was also presented.

The aeroelastic dynamic cases have proven to be more complex than their static counterparts. The authors described a relatively strong dependency of the results with the discretization and convergence thresholds used in the simulations. While the vertical "1-cos" gust results converged with the same discretization used in the static validation cases, the lateral gusts have proven to be a more complex situation, where mesh refinement in a direction leads to the convergence of the quantities in the normal direction (*i.e.*, a chordwise refinement in the aerodynamic grid results in better agreement in the lateral flight dynamics and *vice versa*). Despite the challenges arising from these considerations, the nonlinear aeroelastic results obtained from this exercise provide useful data concerning the structural and flight dynamic behaviour of span-loaded, very flexible aircraft and the challenges associated with their numerical studies.

The capability of the X-HALE to rotate its central tail from vertical to horizontal in flight allows to study the effect of morphing configuration in longitudinal and lateral flight dynamics and their coupling with the structural degrees of freedom.

Future work will focus on improving the understanding of the convergence of the nonlinear aeroelastic codes for lateral dynamics as a function of the applied methods and discretizations used in the context of HALE configurations. Additional non span-constant gust shapes and control inputs have the potential to excite complex interactions between

flight dynamics and aeroelastic degrees of freedom that can only be captured accurately with a combination of suitable numerical methods, models, and discretization procedures. The work carried out in this direction will provide knowledge towards the understanding of gust response specifics for HALE-like configurations, instead of adapting certification rules written with a completely different type of aircraft and application in mind.

ACKNOWLEDGMENTS

A. Del Carre acknowledges the financial support provided by Airbus Defence and Space. He also would like to thank Norberto Goizueta at Imperial College London for his insightful conversations about aircraft flight dynamics. Patricia Teixeira acknowledges the support of CNPq (Conselho Nacional de Desenvolvimento Cientıfico e Tecnologico, Brazil) and the University of Michigan for her academic scholarship.

5 REFERENCES

[1] Cesnik, C. E. S., Palacios, R., and Reichenbach, E. Y. (2014). Reexamined structural design procedures for very flexible aircraft. *Journal of Aircraft*, 51(5), 1580–1591. doi:10.2514/1.c032464.

[2] FAA (2014). Dynamic gust loads - AC 25.341-1. *FAA Advisory Circular*.

[3] Jones, J. R. (2017). *Development of a Very Flexible Testbed Aircraft for the Validation of Nonlinear Aeroelastic Codes*. Ph.D. thesis, University of Michigan.

[4] Jones, J. R. and Cesnik, C. E. S. (2015). Preliminary flight test correlations of the X-HALE aeroelastic experiment. *The Aeronautical Journal*, 119(1217), 855–870. doi:10.1017/s0001924000010952.

[5] Cesnik, C. E. S., Senatore, P. J., Su, W., et al. (2012). X-HALE: A very flexible unmanned aerial vehicle for nonlinear aeroelastic tests. *AIAA Journal*, 50(12), 2820–2833. doi:10.2514/1.j051392.

[6] Murua, J., Palacios, R., and Graham, J. M. R. (2012). Applications of the unsteady vortex-lattice method in aircraft aeroelasticity and flight dynamics. *Progress in Aerospace Sciences*, 55, 46–72. doi:10.1016/j.paerosci.2012.06.001.

[7] Simpson, R. J. and Palacios, R. (2013). Numerical aspects of nonlinear flexible aircraft flight dynamics modeling. In *54th AIAA/ASME/ASCE/AHS/ASC Structures, Structural Dynamics, and Materials Conference*. American Institute of Aeronautics and Astronautics. doi:10.2514/6.2013-1634.

[8] Hesse, H., Palacios, R., and Murua, J. (2014). Consistent Structural Linearization in Flexible Aircraft Dynamics with Large Rigid-Body Motion. *AIAA Journal*, 52(3), 528–538. doi:10.2514/1.J052316.

[9] Del Carre, A. and Palacios, R. (2019). Low-altitude dynamics of very flexible aircraft. In *AIAA Scitech 2019 Forum*. San Diego, California: American Institute of Aeronautics and Astronautics. doi:10.2514/6.2019-2038.

[10] Cesnik, C. E. S. and Brown, E. L. (2002). Modelling of high aspect ratio active flexible wings for roll control. In *43rd Structures, Structural Dynamics, and Material Conference*. Denver, CO: American Institute of Aeronautics and Astronautics. doi: 10.2514/6.2006-1638.

[11] Shearer, C. M. and Cesnik, C. E. (2007). Nonlinear Flight Dynamics of Very Flexible Aircraft. *Journal of Aircraft*, 44(5), 1528–1545. ISSN 0021-8669. doi:10.2514/1.27606.

[12] Su, W. and Cesnik, C. E. S. (2010). Nonlinear Aeroelasticity of a Very Flexible Blended-Wing-Body Aircraft. *Journal of Aircraft*, 47(5), 1539–1553. ISSN 0021-8669. doi:10.2514/1.47317.

[13] Murua, J. (2012). *Flexible aircraft dynamics with a geometrically-nonlinear description of the unsteady aerodynamics*. Ph.D. thesis, Imperial College London.

[14] Katz, J. and Plotkin, A. (2001). *Low-Speed Aerodynamics*. Cambridge Aerospace Series. Cambridge University Press. ISBN 9781107717428.

[15] Simpson, R. J. S., Palacios, R., and Murua, J. (2013). Induced-drag calculations in the unsteady vortex lattice method. *AIAA Journal*, 51(7), 1775–1779. doi: 10.2514/1.J052136.

[16] Guennebaud, G., Jacob, B., et al. (2010). Eigen v3. http://eigen.tuxfamily.org.

[17] Wiener, N. and of Technology (Cambridge, M. M. I. (1950). *Extrapolation, interpolation, and smoothing of stationary time series: with engineering applications*. Technology Press.

[18] Su, W. and Cesnik, C. E. S. (2011). Dynamic response of highly flexible flying wings. *AIAA Journal*, 49(2), 324–339. doi:10.2514/1.j050496.

[19] Su, W. and Cesnik, C. E. S. (2012). Strain-based Geometrically Nonlinear Beam Formulation for Modeling Very Flexible Aircraft. *International Journal of Solids and Structures*, 48, 2349—2360. doi:10.1016/j.ijsolstr.2011.04.012.

[20] Teixeira, P. and Cesnik, C. E. S. (2018). Propeller effects on the dynamic response of HALE aircraft. In *2018 AIAA/ASCE/AHS/ASC Structures, Structural Dynamics, and Materials Conference*. American Institute of Aeronautics and Astronautics. doi: 10.2514/6.2018-1202.

[21] Murua, J., Palacios, R., and R. Graham, J. M. (2012). Assessment of wake-tail interference effects on the dynamics of flexible aircraft. *AIAA Journal*, 50(7), 1575–1585. doi:10.2514/1.J051543.

[22] Melin, T. (2013). Tornado. *KTH, Stockholm, Sweden, Masters Thesis and continued development. http://www.flyg.kth.se/divisions/aero/software/tornado*.

[23] Marco, A. D., Duke, E., and Berndt, J. (2007). *A General Solution to the Aircraft Trim Problem*. doi:10.2514/6.2007-6703.

[24] Broyden, C. G. (1965). A class of methods for solving nonlinear simultaneous equations. *Mathematics of computation*, 19(92), 577–593.

[25] Etkin, B. (1982). *Dynamics of flight: stability and control*. John Wiley & Sons Australia, Limited. ISBN 9780471089360.